December 2015 Technical Report: KUL/ESAT/PSI/1504

Investigating the need for additional kV imaging in marker based prostate motion tracking using the MV treatment beam

H. Van Herck, W. Crijns, P. Slagmolen,
T. Depuydt, K. Haustermans and F. Maes

PSI

Kasteelpark Arenberg 10 box 2441
3001 Leuven, Belgium

KU LEUVEN

Telephone: +32-(0)16-32.17.13 Fax: +32-(0)16-32.17.23 http://www.esat.kuleuven.be/psi

Investigating the need for additional kV imaging in marker based prostate motion tracking using the MV treatment beam

H. Van Herck[1,2,3], W. Crijns[2,3], P. Slagmolen[1,3], T. Depuydt[2,3], K. Haustermans[2,3] and F. Maes[1,3]

[1]KU Leuven, Dept. of Electrical Engineering, Processing Speech and Images (ESAT/PSI), Kasteelpark Arenberg 10, 3001 Leuven (Heverlee), Belgium
[2]KU Leuven, Dept. of Oncology, Laboratory of Experimental Radiotherapy, UZ Leuven, Herestraat 49, 3000 Leuven, Belgium
[3]KU Leuven, Medical Imaging Research Center, UZ Leuven, Herestraat 49, 3000 Leuven, Belgium

April 2015

Abstract

Purpose: In radiotherapy treatment of prostate cancer patients, volumetric modulated arc therapy (VMAT) exhibits both an improvement in dose distribution and a decreased treatment time with respect to 3D conformal radiotherapy. With markers implanted in the patients prostate, intra-fraction prostate motion can be tracked using only the treatment beam. However, complex multi-leaf collimator (MLC) modulation schemes can result in a high degree of marker invisibility in the acquired MV images and a diminished tracking accuracy. The use of additional intra-fraction kV imaging may provide a solution. In this work, its influence on marker based prostate motion tracking is investigated.

Methods: A novel, fast detection algorithm was developed in-house to detect the projections of the implanted fiducial markers on MV images acquired intra-fraction using the treatment beam. It consists of three steps: image preprocessing, marker position estimation and marker detection. The detected marker positions were then used as inputs of a reconstruction algorithm that finds the 3D marker locations and their corresponding intra-fraction motion. Validation of detection and reconstruction was performed on a dynamic pelvis phantom, where both drift (1 mm and 3 mm) and jump (2 mm) motion patterns were applied to the phantom. Marker invisibility in the MV projection images was simulated by taking into account the positions of the MLC edges as calculated in the patients treatment plan. A pretreatment protocol was also developed to indicate the need for additional kV imaging and the frequency of kV imaging was varied to study its influence on reconstruction accuracy during marker MV invisibility.

Results: Mean 2D detection error norms were smaller than 0.8 mm ($\pm$ 0.9 mm) for all phantom motion patterns, with at least 97% of all visible marker positions being detected. For the 3D marker location reconstruction method, the RMS values of the 3D reconstruction error norms were calculated. This resulted in RMS values smaller than 0.8 mm for the applied drift motion and values smaller than 1.5 mm for the applied jump motion. When accounting for marker MV invisibility, submillimeter mean reconstruction accuracy was lost for the 3 mm drift and 2 mm jump motion patterns without additional kV imaging. Single marker submillimeter mean reconstruction accuracy was again obtained by incorporating at most 38 additional kV images for one full gantry rotation, depending on the type of motion pattern.

Conclusions: With MV-only imaging, a combination of the proposed detection and reconstruction methods results in submillimeter reconstruction accuracy when marker projections are visible inside the projected MLC boundaries. In case of invisible markers, only a limited number of additional kV images needs to be acquired to retain this accuracy.

1 Introduction

In radiotherapy (RT) treatment of cancer patients suffering from prostate cancer, among others, static gantry intensity-modulated radiation therapy (IMRT) has clearly proven its superiority compared to 3D conformal RT when considering organ-at-risk (OAR) sparing and delivered dose distribution [1]. Its successor, volumetric modulated arc therapy (VMAT) [2], generally exhibits an even better improvement with respect to dose distribution, along with a highly decreased treatment time [2, 3]. During VMAT, treatment of a prostate tumor consists of continuous irradiation during a 360 degrees rotation of the gantry. Although the shorter treatment time is expected to reduce the effect of intra-fraction prostate motion on the effective delivered dose, it does not eliminate it. Both Langen *et al.* [4] and Xie *et al.* [5] reported that typical intra-fraction prostate motion patterns include continuous drift and transient excursion as well as variations of the two. General pelvic musculature relaxation, gradually moving rectal content and bladder volume changes were mentioned as probable causes for the drift motion, while excursions probably occurred because of peristalsis. Left-Right (LR) prostate motion was also much smaller compared to anterior-posterior (AP) and inferior-superior (IS) motion and there appeared to be a clear correlation between the two latter components. Tracking this prostate motion during a treatment session can substantially reduce target safety margins [6, 7] and thus helps in sparing healthy tissue around the tumor. Typically, implanted fiducial markers are used to represent prostate and tumor motion. In patients, marker migration is assumed to be negligible [16], so that inserted markers with fixed locations serve as a good model for rigid motion. Tracking 3D prostate motion during VMAT then relies on tracking the fiducial markers, which consists of two components: detecting the 2D marker projections on MV images and reconstructing the 3D marker locations using their 2D projections on an imager mounted on a rotating gantry.

Methods based on template matching are often proposed to detect marker projections in 2D treatment images. Nederveen *et al.* [8] use a marker extraction kernel (MEK) with variable height and width that resembles the local image appearance of the implanted markers. The actual marker location is retrieved by convolving the MEK with the image within a small window around the expected marker location as estimated from prior CT data and searching for the maximal response, while varying the orientation of the MEK. Mao *et al.* [9], on the other hand, used precalculated marker cross-sections and maximize the correlation coefficient between a markers projection and its corresponding cross-section. The same criteria were also used by Azcona *et al.* [10]. Alternatives to template matching include the use of the Laplacian of Gaussian function combined with an automatically determined intensity threshold [11] and advanced computer vision techniques including principal component and linear discriminant analysis in combination with a set of training images of detected markers [12]. However, these detection methods either require prior knowledge about marker orientation and dimensions [8, 9, 10, 12] or result in unsatisfactory detection results when applied to low contrast MV images in our institution [11].

To reconstruct a marker's 3D location, Poulsen *et al.* [13] proposed a method based on a 3D Gaussian probability density function (PDF) and its intersection with the ray line between the radiation source and the marker's projected position on the imager. Similarly, Li *et al.* [14] presented a Bayesian framework to estimate the PDF of the 3D marker location by optimizing a maximum a posteriori estimator based on previous marker projections. However, both approaches require pretreatment projection data to construct the PDF and thus an additional imaging session before the actual treatment. A reconstruction method that does not require prior information was proposed by Slagmolen *et al.* [15] for IMRT. It calculates a set of 3D marker candidate locations from subsequent projection images and finds the optimal 3D marker location by combining 2D image intensity information and information about the 3D geometric configuration of all implanted markers. An expansion of this method to 3D location reconstruction during VMAT may prove promising.

Tracking markers during VMAT is complicated by multileaf collimator (MLC) leaf motion, blocking marker projections on the MV treatment images. This can result in long periods of marker invisibility and consequently large errors in the reconstructed marker locations and thus in the motion inferred from them, inhibiting reduction of the margins. Performing additional, simultaneous kV imaging during treatment may prove an adequate solution.

In this paper, we investigate the accuracy and feasibility of fiducial marker tracking in prostate tumors by using a novel in-house developed fiducial marker detection and reconstruction algorithm. Initially, MV-only tracking is examined, without and with marker invisibility due to MLC leaf motion. Next, the influence of additional kV imaging on marker tracking is investigated. In an attempt to limit the effective dose, a method is proposed to indicate the need for additional kV imaging based on the leaf positions during treatment and the marker locations in the planning CT. Before actual treatment, the

method calculates the position and number of gantry angles that require kV imaging. Imaging during treatment can then be modified accordingly to improve reconstruction results.

This paper is organized as follows: the proposed detection and reconstruction method are discussed in more detail in Section 2, along with a detailed description of the performed phantom experiments and the addition of partial kV imaging. Section 3 then describes the reconstruction results for both MV-only and orthogonal kV/MV imaging. The value of additional kV imaging for reconstruction is also investigated for the application of realistic treatment plans. Some remarks are discussed in Section 4 and finally Section 5 concludes the text.

2 Materials and methods

2.1 Phantom setup and imaging

All experiments and simulations discussed in this study were performed on a dynamic pelvis phantom (CIRS Model 008P Dynamic Pelvis Phantom, CIRS Inc., Norfolk, VA, USA). The prostate is embedded in a cubical insert that also contains 4 cylindrical gold markers (5 mm length, 1 mm diameter) positioned symmetrically around the prostate center . This insert follows a circular motion in the sagittal AP-IS plane, according to a rotating disk which is driven by a linear rod linked to an external, linearly moving actuator (Figure 1). There is no motion in the LR direction. The actuator's exact motion can be programmed by the phantom's motion software and the ground truth motion of each marker individually can be calculated from the known phantom's geometry. This setup is a good approximation for real prostate motion, as was discussed in Section 1 and literature [4].

Imaging was performed over the course of one 360^o rotation (60 s) of a 10 MV Varian TrueBeam linac (Varian Medical Systems, Palo Alto, CA, USA) with a dose rate of 600 MU/min. MV images were acquired by using the treatment beam and an IDU20 MV imager with an imaging matrix of 1024×768 pixels and an active imaging area of 40×30 cm^2 (pixel size of 0.392×0.392 mm^2). The source-to-axis distance (SAD) in our setup was 100 cm and the source-to-imager distance (SID) was 145 cm, with a collimated field size of 14.5×11 cm^2. The MV imaging frame rate was 4.3 images per second, resulting in about 260 images over the entire arc rotation (Figure 2).

2.2 Marker detection

The MV images were first pre-processed to remove artifacts. The average of each row and column was subtracted from the original image to remove linear horizontal and vertical offsets, followed by a Wiener filter [17] to reduce high frequency noise. Additional unsharp masking was performed with a 20 x 20 pixel averaging filter to extract all smaller shapes resembling a projected marker. From the resulting image, a region of interest (ROI, 60 x 60 pixels) was retained for every marker. The center of each ROI was found as the projection onto this MV image of the 3D location of the corresponding marker in the planning CT. Canny edge detection [18] was then applied to each of these ROIs separately, retaining the clearest edges. The processed ROIs were gathered into one image, which was saved as a list of contiguous regions, by using the *regionprops* function in MATLAB (The Mathworks Inc., Natick, MA, USA). Each contiguous region was delimited by edges obtained by performing edge detection and its center and area were computed. Regions with less than 5 and more than 200 pixels were discarded.

The proposed detection algorithm consists of finding the 2D positions of marker projections in every MV image based on incrementally adjusted 2D position estimates. The position estimate of a marker was updated for every new projection image. For a positive marker detection in the previous projection image, the marker's position estimate in the current projection was set equal to that previously detected position. If the marker was not found in the previous projection, its position estimate was kept constant. Failure to detect the marker in three consecutive projection images resulted in a reset of the position estimate to the marker's projected planning CT coordinates. In the case of two coinciding markers, their position estimates were offset from the position of coincidence in different directions based on the position of their corresponding projected CT coordinates. For a high frame rate, projected marker positions can coincide in several consecutive projection images before drifting apart again. The offset in position estimates during this time ensured detection of the correct marker position after coincidence.

For each marker, the optimal 2D position in the MV image was found by comparing the marker's position estimate to the position of the center of every contiguous region in the list mentioned earlier. To find the best match, our algorithm searched for the region closest to the position estimate, taking into account the presence of regions at the position estimates of the other markers. The optimization

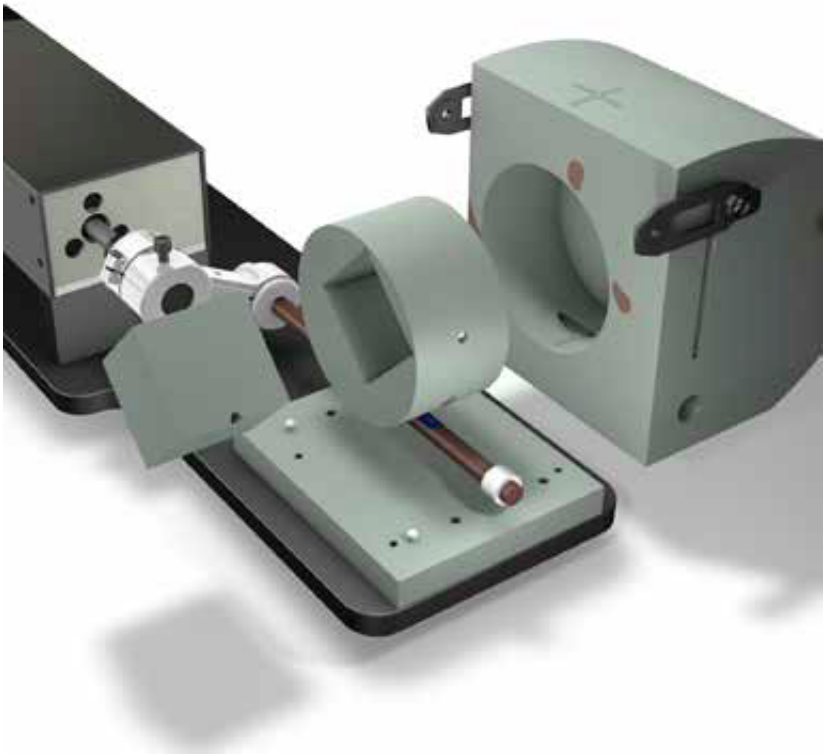

Figure 1: Dynamic motion phantom consisting of a linearly moving rod that drives a rotating disk that contains the cubical insert with the prostate and 4 gold markers. Image courtesy of CIRS Inc.

.

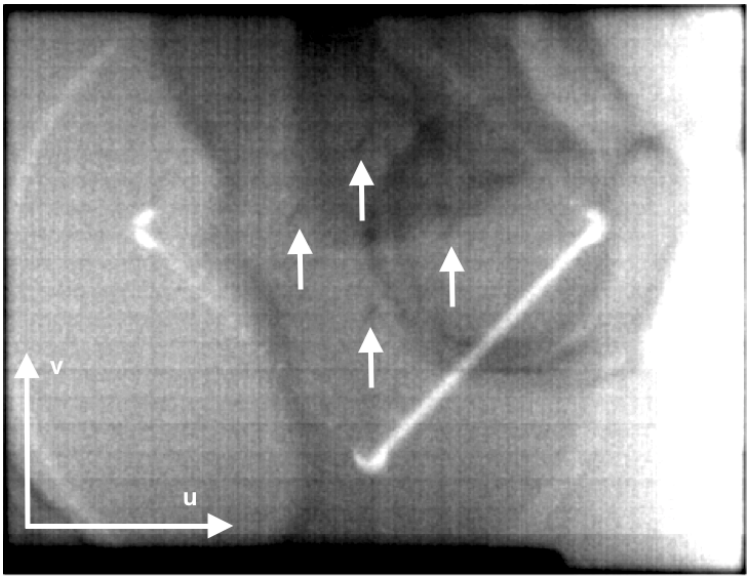

Figure 2: MV projection image at 270^o gantry angle containing the four markers (indicated by white arrows) inside a cubical insert of which the center coincides with the phantom's prostate. The edges of the cube are also visible here as white lines, as well as the edges of the rotating disk containing the cube insert.

criterion that was used, is the following [19]:

$$\max_{r,s\in\mathcal{R}}\left[\lambda\times(1-||e_i-r||/T_1)+\sum_{n=1}^{N}(1-\delta(n-i))\times(1-||(e_n+[r-e_i])-s||/T_2)\right] \quad (1)$$

with r and s the 2D positions of a contiguous region's center, $\mathcal{R}$ the set of all regions in the processed MV image, e_i the position estimate of marker i and N the total number of markers. $\delta(x)$ is the Dirac-delta function. T_1 and T_2 are thresholds for the distances between, respectively, the position estimate of the considered marker e_i and its possible matching region r and the translated position estimate of every other marker $e_n + [r - e_i]$ and their possible matching regions s. Parameter optimization was performed on a training set and yielded optimal values for T_1 and T_2 of 20 and 13 pixels, respectively. The optimal value for the merging parameter λ was found to be 1.2. Maximization of Eqn. 1 was performed exhaustively for all contiguous regions in the processed MV image. Execution speed scales quadratically with the number of regions. As only a limited number of regions (an average of 8 for our experiments) still remain after the preprocessing steps described earlier, execution speed is therefore not an issue. Because of the value of T_1, a marker was classified as undetected when there was no region center found within a 20 pixel radius of the marker's position estimate. Its current position was then set equal to that of the previous detection. Consequently, this position is also used as the marker's position estimate in subsequent projection images, until a new successful detection occurs.

2.3 MV-only marker location reconstruction

Each 2D marker position has a horizontal and vertical coordinate on the MV image, represented by (u, v), where u increases from left to right and v increases from top to bottom of the image (Figure 2). 3D coordinates x, y and z represent the LR, AP and IS dimensions respectively, with the linac's isocenter being the system origin. The direction of x coincides with that of u in the 2D MV image at 0^o gantry angle (i.e. increases from the patient's right to left), y increases from anterior to posterior and z from inferior to superior. Projecting a 3D coordinate $x(x, y, z)$ to a 2D coordinate $m(u, v)$ on the pth MV projection image is given by [20]:

$$u = \mathrm{SID}\times\frac{x\cos\theta_p+y\sin\theta_p}{\mathrm{SAD}-x\sin\theta_p+y\sin\theta_p} \quad (2)$$

$$v = \mathrm{SID}\times\frac{-z}{\mathrm{SAD}-x\sin\theta_p+y\sin\theta_p} \quad (3)$$

with θ_p the pth gantry angle and SID and SAD the source-to-imager and source-to-axis distances, respectively. Reconstruction of the 3D intra-fraction location of each marker was performed by minimizing the optimization criterion of Yue *et al.* [21], with a number of adjustments described below.

A regularization term was added by Yue *et al.* [21] in the form of a 3D predetermined motion prior. This motion prior was initially determined by a large amount of patient data and was calculated as the mean of the most frequently occurring prostate displacements [21]. We found that a zero motion prior accomplished comparable results and solely acted as a regularization limiting the magnitude of the translation between consecutive reconstructed 3D marker locations. This is feasible for prostate motion, because mostly small motion occurs between consecutive MV projections acquired during arc treatment [4].

A 3D merging vector $\alpha(\alpha_x, \alpha_y, \alpha_z)$ between the motion conditional probability term and the motion prior term was used. The directional components α_x, α_y and α_z were independent and had the values 0.5, 0.001 and 0.001 for the LR, AP and IS dimensions respectively. The combination of a relatively large value for α_x and a zero motion prior strongly enforces a constant LR marker location. Furthermore, the last two terms in the denominator of Eqn. 3 can be neglected with respect to the source-to-axis distance SAD. The coordinate z consequently depends almost exclusively on v. A small value of α_z then allows motion in the v-direction to directly propagate to the reconstructed z-dimension. Eqn. 2 represents an underdetermined system for x and y, with one known coordinate u. This is partly solved by enforcing a constant LR (i.e. x) marker location, but difficulty with AP (i.e. y) reconstruction still exists at gantry angles where the AP motion was (nearly) parallel to the imaging projection ray. Motion in this direction can not be distinguished in the projection image, leading to unreliable reconstructions. The reconstructed location was therefore forced to remain constant around gantry angles where the projection

ray was parallel to the AP motion. In particular, for the MV imager, this occurs at gantry angles of 180^o, 0^o and -180^o. A range of 10 gantry angles (i.e. 15^o) before and after these angles was used.

The moving window strategy used by Yue *et al.* [21] was adapted to allow for real-time tracking. Our algorithm calculated the reconstruction at gantry angle θ_p as the mean of the reconstructions at angles θ_{p-2} to θ_p. Undetected marker locations were set equal to their previously reconstructed locations. To improve tracking speed and accuracy, the Newton variant of gradient descent [22] was used in combination with a line search algorithm [23] for the step size.

2.4 Phantom experiments

Initially, MV projection images of the static phantom were acquired during a 360^o arc. No motion was applied to the phantom to examine the propagation of 2D marker detection errors on the final reconstruction results and the size of possible base reconstruction inaccuracies.

Next, different motion patterns were applied to the phantom in one arc rotation, where the AP location of the phantom's prostate center was used as reference point. A 1 mm motion then signified a prostate center motion of 1 mm in the AP dimension. The corresponding motion in the IS dimension was determined by the size of the rotating phantom disk containing the prostate and the distance from the prostate center to the center of the disk. To simulate realistic clinical situations, investigated phantom motions included two continuous drifts of 1 mm and 3 mm (posteriorly and inferiorly) and one motion pattern with alternating jumps of the prostate center (see Figure 3). The jumps were simulated to occur around challenging gantry angles (-135^o, -90^o, 0^o, 45^o, 90^o and 180^o for an arc rotation from 180^o to -180^o) where the projection ray was either horizontal, vertical or exactly in between. As motion of more than 5 mm is less likely to occur in prostate [4], we limited the size of the jumps to 2 mm at the prostate center. The symmetrical marker placement around the prostate center then resulted in jumps of the inserted markers ranging from 0.5 mm to 4.5 mm. Figure 3 shows both the AP and IS components of the applied motion patterns. There is a clear relation between the magnitude of the motions in the IS and AP dimensions, in accordance with real prostate motion [4, 5, 24].

Additionally, two more motion patterns with larger, less realistic jumps of 5 mm and 8 mm at the prostate center, resulting in jumps of 1.2 to 18 mm for the separate markers, were examined to assess the capability of our reconstruction algorithm to cope with fast moving markers. Instead of using the detection algorithm for these jumps, detected marker positions were simulated by adding white Gaussian noise to the projected ground truth locations. The mean and standard deviation of the 2 mm jump motion detection results were used for the statistical distribution of the noise. Reconstructed marker locations of these jump motions were not kept constant around gantry angles 180^o, 0^o and -180^o, since that would influence the speed with which the reconstructed marker location follows the ground truth location.

2.5 MV reconstruction with additional kV imaging

To simulate real-time intra-fraction tracking of implanted prostate markers, marker invisibility was introduced based on an actual VMAT treatment plan of a prostate cancer patient treated at our institute. For each control point of the plan, the MLC leaf positions were projected onto the MV image acquired for our dynamic prostate phantom at the corresponding gantry angle. Marker projections covered by the MLC leafs were considered to be invisible at that gantry angle. The reconstructed locations of these marker projections were set equal to their previous location.

For high complexity MLC modulations, marker projections can remain invisible for a large percentage of the treatment time, resulting in an unreliable reconstruction. This can be alleviated by the use of additional kV imaging. Orthogonal kV/MV imaging at every gantry angle greatly increases the reconstruction accuracy. Therefore, kV/MV reconstruction was used as a reference in our experiments, next to the ground truth motion. As our Varian TrueBeam system did not allow for simultaneous kV/MV imaging, we simulated the detection of marker positions in a virtual kV image orthogonal to the MV image by projecting their 3D ground truth locations and adding normally distributed white noise (0.5 mm $\pm$ 0.5 mm) to account for kV detection errors.

With additional kV imaging, the problem of indistinguishable AP motion in the MV images (i.e. AP motion parallel to the projection ray, see Section 2.3) could be solved by performing 3D marker reconstruction on the orthogonal imager. Hence, kV-only reconstruction was performed in a range of 15^o before and after gantry angles of 0^o and 180^o and MV-only reconstruction in a range of 15^o before and after $\pm 90^o$. However, while improving the reconstruction accuracy, additional kV imaging during treatment delivers a higher dose to the patient. Performing additional kV imaging during the entire 360^o

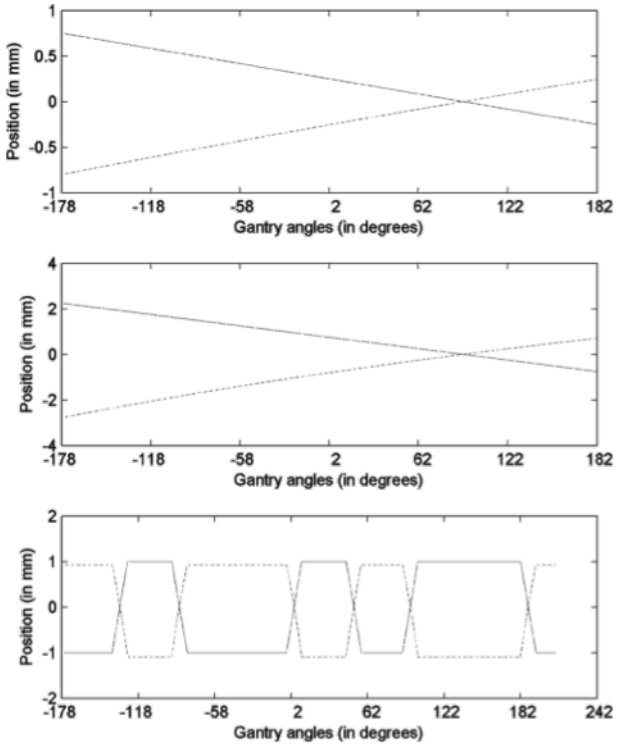

Figure 3: Investigated motion patterns of the phantom prostate center with realistic magnitudes, for a complete arc rotation from -180 to 180 gantry angles. The AP (solid) and IS (dashed) positions for the 1 mm and 3 mm drift and 2 mm jump motion are depicted from top to bottom respectively.

arc can be compared to a full CBCT, of which the integral dose during a treatment delivery should not be ignored [25]. To limit this additional dose, a compromise between MV-only imaging and complete kV/MV imaging has to be found.

We propose a method that can be performed pretreatment, to determine when additional kV imaging is advisable during treatment. It consists of projecting the 3D locations of each marker in the planning CT into the MV beams eye view at the gantry angle of every control point in the treatment plan, resulting in acceptable 2D estimates of the real marker projections at every control point. For each control point and each marker, visibility of the estimated marker location with respect to the projected MLC leaf positions was determined. Ranges of gantry angles at which the estimated marker locations would be obscured by the MLC leafs and hence invisible in the MV images were retained. During arc rotation, additional kV imaging was then simulated at gantry angles within these ranges only.

Depending on the visibility of the actually detected marker positions in the MV images during arc rotation and their anticipated visibility based on the initially estimated marker locations, different situations can be distinguished in our experiments. If both the estimated and the actual marker locations were visible, MV-only reconstruction was performed as discussed in Section 2.3. If the estimated location was invisible while the actual location was visible, orthogonal kV/MV reconstruction was performed by finding the closest 3D point between the kV and MV projection rays. If the actual location was invisible while the estimated location was visible, no kV imaging would be performed for this gantry angle and the reconstruction was kept equal to the previously reconstructed location. Also if both the estimated and the actual locations were invisible, the previously reconstructed location was kept in our experiment (although kV-only reconstruction could have been performed as well in this case).

Finally, the influence of the frequency of additional kV imaging in the proposed scheme for kV/MV imaging based on marker visibility was also examined. The size of the interval between gantry angles at which a kV image was used to update the reconstructed marker location during invisibility of the CT markers was varied from 1 (kV imaging used for all gantry angles of CT marker invisibility) to 10 (kV imaging used once every 10 gantry angles of CT marker invisibility). This was initially examined for all markers separately, with different marker visibility schemes. In practice, multiple markers are available for the reconstruction. Therefore, the influence of kV imaging frequency on the mean reconstructed

marker location was also investigated, with respect to the mean ground truth marker location.

3 Results

3.1 Marker detection

The proposed 2D marker detection algorithm was applied to the acquired MV images of the dynamic prostate phantom with realistic motion patterns as described above (Figure 3). Ground truth 2D marker positions were obtained by manual indication on the MV images. Detection errors were calculated as the 2D distance between detected position and ground truth. Mean detection errors, averaged over all markers, were 0.75 ± 0.86 mm (mean ± standard deviation), 0.69 mm ± 0.75 mm, and 0.77 mm ± 0.9 mm for 1 mm drift, 3 mm drift, and 2 mm jumps respectively. The corresponding detection rates (i.e. percentage of detected vs. total number of markers) were 98%, 97%, and 99% respectively. The detection errors were smaller than 1 mm for 80%, 83% and 81% of the detected markers respectively. For each projection image in which all markers were detected, the center of mass (i.e. center of the markers) and its detection error were also calculated. These errors were 0.51 ± 0.4 mm, 0.42 ± 0.34 mm, and 0.5 ± 0.47 mm for the 1 mm drift, 3 mm drift and 2 mm jumps respectively. These are considerably smaller than the individual marker errors as single inaccurate marker detections are averaged out. The center of mass moves along the overall direction of motion all four markers individually and therefore gives a good indication of the projected global prostate motion.

3.2 MV-only marker location reconstruction

The detected 2D marker positions discussed in Section 3.1 were used for the reconstruction of the drift and jump motion patterns. RMS values of the reconstruction errors in AP and IS dimensions were smaller than 0.7 mm for the drift motions and smaller than 1.3 mm for the jump motion. As the RMS values of the LR reconstruction errors were smaller than 0.02 mm but not completely zero, RMS values of the 3D reconstruction error norms were also calculated for these three motion patterns. They were smaller than 0.8 mm for the 1 mm and 3 mm drift and smaller than 1.5 mm for the 2 mm jump motion. The larger errors of the jump motion originated mainly from the latency of the reconstructed marker location with respect to the ground truth location at 0^o gantry angle, caused by keeping the reconstructed marker location constant at angles where the projection ray is parallel to the AP motion. Figure 4 shows the ground truth and reconstruction of the 3 mm drift motion in both the AP and IS dimension, for two of the four markers inserted in the prostate phantom. Reconstruction errors were generally below 1 mm, except for a few isolated spikes where high errors occurred. Because the reconstruction is strongly affected by the detection accuracy, large detection errors will result in large reconstruction errors. For instance, the detection error of the first marker (Figure 4, top left) was 3.9 mm at the peak in the error at 90^o gantry angle and 3.2 mm at the peak around -33^o, causing the error in the AP reconstruction to spike to 3 mm. The AP reconstruction of the second marker (Figure 4, top right) illustrates the rationale for keeping the AP marker location fixed around a gantry angle of 0^o, as discussed in Section 2.3. Here, the reconstruction had already started to deviate from the ground truth before the range of gantry angles around 0^o within which its AP location was kept fixed. The error would have been much larger if a constant AP location was not enforced within this range.

For the 5 mm and 8 mm jump motions, RMS values of the reconstruction errors were again calculated for the AP and IS dimensions and for the 3D norm. They were smaller than 1.4 mm, 1.1 mm and 1.8 mm respectively for the 5 mm jump motion pattern and smaller than 1.8 mm, 1.6 mm and 2.1 mm respectively for the 8 mm jump motion pattern. Figure 5 shows the reconstruction results of the 8 mm jump motion for two markers in the AP and IS dimensions. A latency in the AP reconstruction occurs at the positions of the jumps. This latency exists because of the moving window average, where every reconstruction is the mean of the current and previous two reconstructions. However, not implementing this smoothing step would allow instability in the reconstructed marker location, which can lead to large reconstruction errors. Finally, because the originally reconstructed marker locations are used around gantry angles 180^o, 0^o and -180^o, spikes can clearly be seen in the AP components of the reconstructions around these angles, which confirms the need for keeping the reconstructed marker positions fixed here.

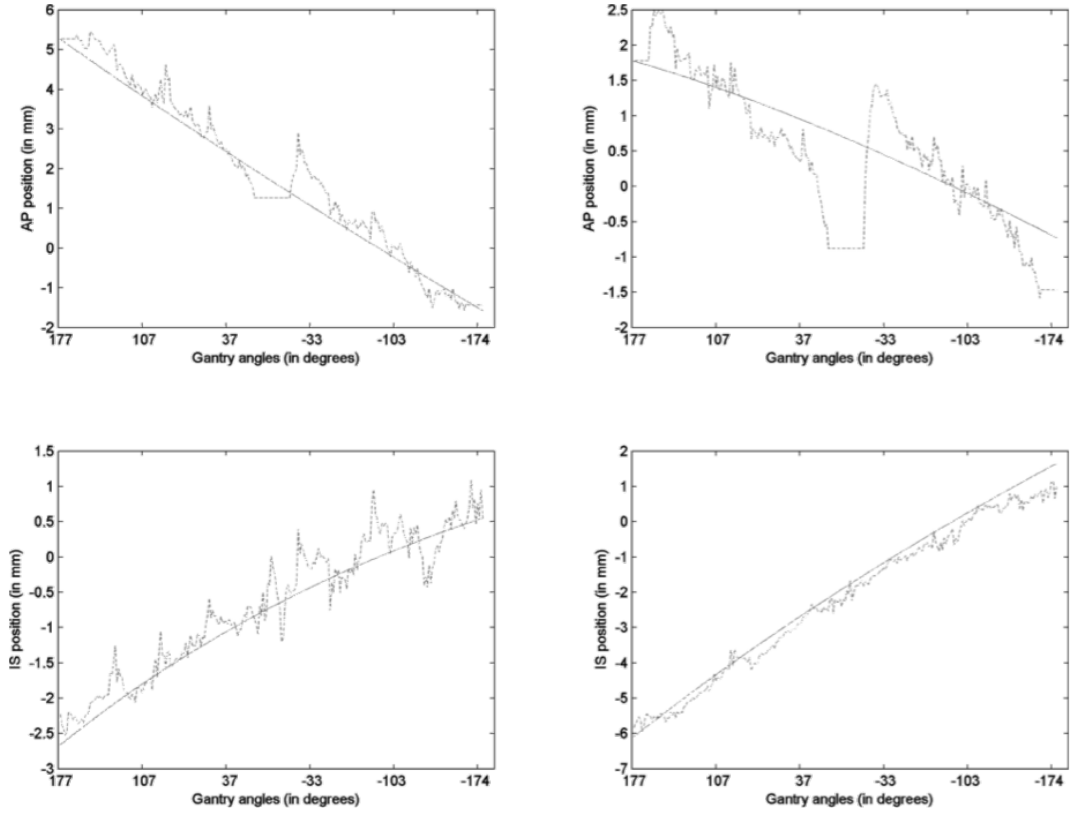

Figure 4: Reconstructed AP (top row) and IS (bottom row) marker locations for two inserted markers (left and right column) for the 3 mm drift motion of the phantom prostate center. The ground truth position (solid) and its reconstruction (dashed) are depicted.

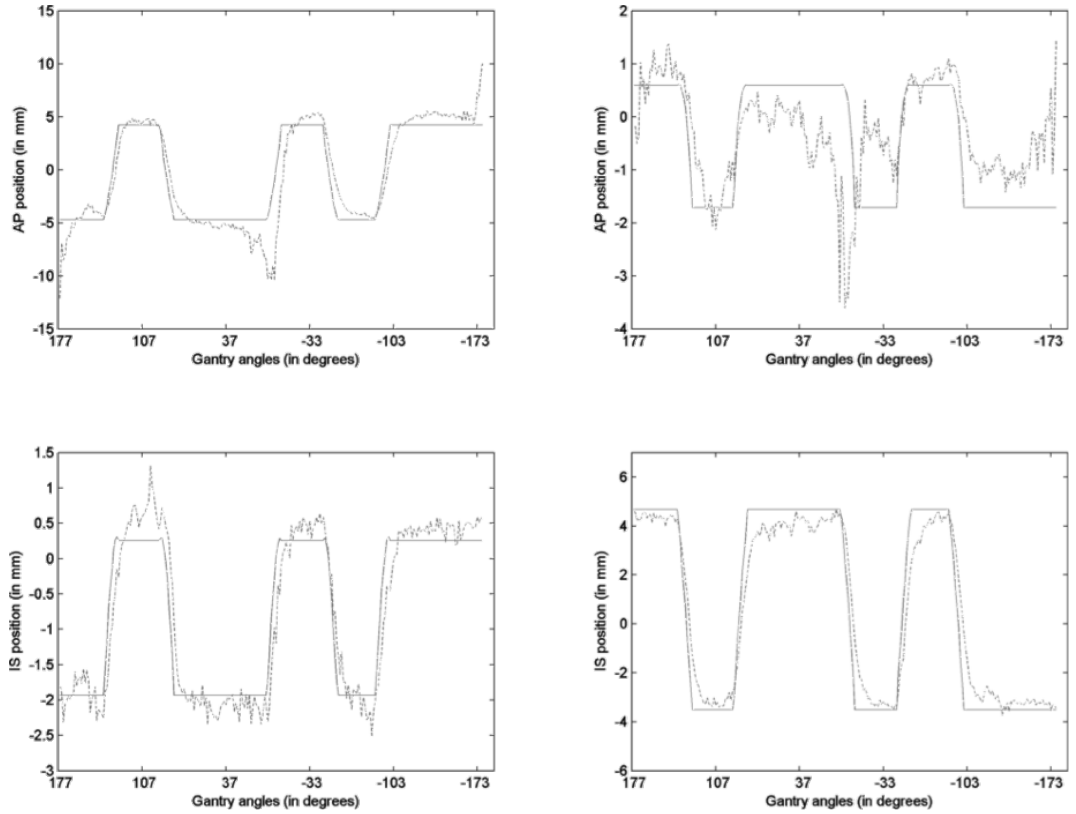

Figure 5: Reconstructed AP (top row) and IS (bottom row) marker locations for two inserted markers (left and right column), for the 8 mm jump motion of the phantom prostate center. The ground truth position (solid) and its reconstruction (dashed) are depicted. Contrary to Figure 4, the reconstructed location around gantry angles where the MV projection ray and motion direction are parallel (i.e. 180^o, 0^o and -180^o) was not kept constant.

3.3 MV reconstruction with additional kV imaging

The realistic motion experiments with the phantom were used to simulate the clinical situation, with modulated collimator leaves obtained from the actual VMAT treatment plan of a patient treated at our institute. The expected visibility of each of the four markers inside the projected leaf apertures based on their 3D CT position was reduced to 40%, 33%, 42% and 28% of the gantry angles of a full arc rotation.

Figure 6 shows the reconstructions in AP and IS dimension of the first marker for the 3 mm drift motion after accounting for the VMAT treatment plan when detecting the marker's position in the MV projection images. Four different curves are shown: the ground truth marker location and the three reconstructions obtained by using the MV images only (i.e. no kV imaging), using additional kV imaging at every gantry angle (i.e. full kV imaging) and using additional kV imaging at selected gantry ranges based on expected marker invisibility as explained in Section 2.5 (i.e. selective kV imaging). The marker's visibility on the MV projection images at each gantry angle is also represented. Qualitatively, it can be seen that using MV imaging only and no kV imaging yields the least accurate reconstruction results. However, in this case the reconstruction errors were only marginally larger in comparison to the other methods, mainly because the simulated marker motion did not exhibit large instantaneous changes in magnitude. In contrast, the use of additional kV imaging at each gantry angle was expected to yield the best results, as much more 2D projection data is available for the reconstruction. Selective kV imaging based on expected marker invisibility showed comparable results as those obtained with full kV imaging and its reconstruction alternated between the results of the other two methods. For all simulated prostate motions (i.e. 1 mm and 3 mm drift and 2 mm jumps) and all markers, mean and RMS values of the reconstruction error norms were calculated and presented in Table 1. Global results were the same as those already witnessed in Figure 6, i.e. using additional kV imaging for all gantry angles yielded the smallest reconstruction errors, while no additional kV imaging yielded the largest. As expected, reconstructions with selective kV imaging were generally better than without kV imaging and worse than with full kV imaging.

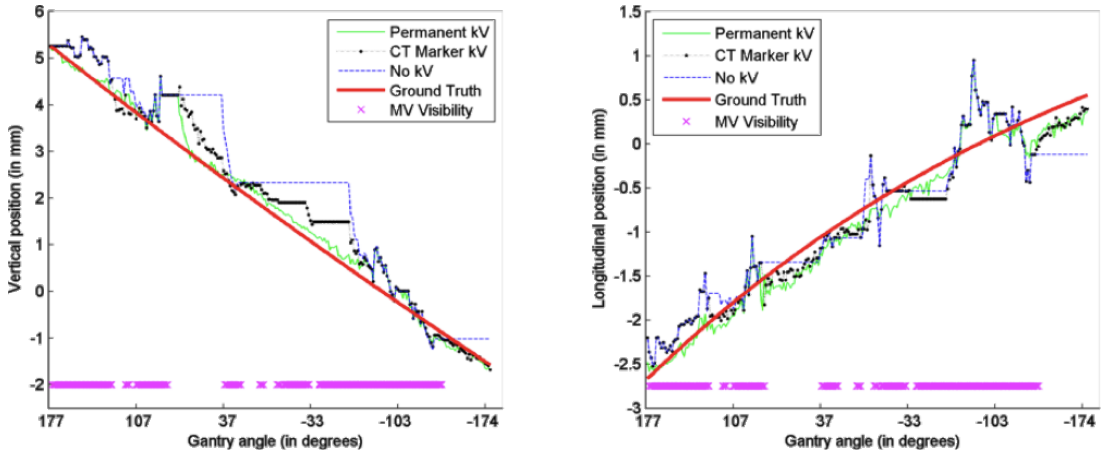

Figure 6: Reconstructed AP (left) and IS (right) marker location for one of the inserted markers, for the 3 mm drift motion of the phantom prostate center. Both figures contain the ground truth marker location (red, thick) and the reconstruction obtained by using only MV imaging and no kV imaging (blue, dashed), using full kV imaging (green, solid) and using selective kV imaging based on projected CT marker invisibility (black, points). For the latter, MV-only reconstruction was used for gantry angles at which the marker was expected to be visible (magenta, crosses) and orthogonal kV/MV reconstruction for gantry angles at which the marker was expected to be invisible (empty areas between magenta crosses).

Reconstruction results obtained by varying the frequency of additional kV imaging are depicted in Figure 7. Values of the reconstruction error norms were calculated and averaged for all gantry angles and markers for each of the three motion patterns separately. As can be expected, mean errors decrease as the interval between kV images decreases, i.e. when more additional kV images are used for 3D marker reconstruction. Especially the larger jump motion benefits most from additional kV imaging. For all three applied motion patterns, mean error norms over all markers and gantry angles are smaller than 1 mm for all investigated kV imaging schemes. This means that, depending on the clinical application, the degree of marker blockage by the MLC and the required reconstruction accuracy, the use of additional

Table 1: Mean and RMS values of 3D reconstruction error norms for the simulated typical prostate motions (1 mm and 3 mm drift and 2 mm jumps). Errors were calculated for all four markers while varying the method that determines the gantry angles for which additional kV imaging was used: permanent, based on CT marker projection invisibility and none.

		Mean/RMS reconstruction error norms (mm)			
Motion type	kV Imaging	Marker 1	Marker 2	Marker 3	Marker 4
Drift 1 mm	Full	0.29/0.19	0.39/0.21	0.37/0.21	0.30/0.16
	Selective	0.32/0.21	0.52/0.30	0.35/0.21	0.27/0.14
	None	0.53/0.34	0.58/0.31	0.71/0.43	0.41/0.23
Drift 3 mm	Full	0.32/0.19	0.49/0.28	0.33/0.18	0.32/0.17
	Selective	0.43/0.25	0.51/0.30	0.40/0.22	0.29/0.16
	None	0.75/0.44	1.03/0.57	0.78/0.47	0.58/0.35
Jumps 2 mm	Full	0.49/0.33	0.52/0.35	0.62/0.40	0.38/0.24
	Selective	0.72/0.55	0.60/0.40	0.62/0.41	0.37/0.24
	None	1.42/0.96	1.04/0.64	1.32/0.83	0.70/0.42
		Number of kV images used			
	kV Imaging	Marker 1	Marker 2	Marker 3	Marker 4
	Full	257	257	257	257
	Selective	98	161	156	189

kV imaging can be limited to a large extent. For instance, the mean error of 0.62 mm obtained for marker 3 for the jump motion pattern using the selective kV imaging scheme as listed in Table 1 was obtained using 156 additional kV images. A more detailed analysis shows that a mean error of less than 1 mm can already be obtained using only 22 kV images.

Analogous to the 2D marker detection results, using the mean reconstructed location of the four markers yielded even better tracking results, as also depicted in Figure 7. The influence of additional kV imaging was comparable, but the reconstruction errors of the mean marker location were around 30% smaller than the mean of the reconstruction errors of the separate markers. More accurate tracking can thus be achieved with multiple implanted markers, even when one or more marker projections are occluded by the collimator leaves. For instance, mean error norms for the mean marker location compared to its ground truth location for the 1 mm and 3 mm drift motion and the 2 mm jump motion were 0.37 mm, 0.61 mm and 0.97 mm respectively without the use of additional kV imaging, which is a clear improvement over the errors for the separate markers as listed in Table 1.

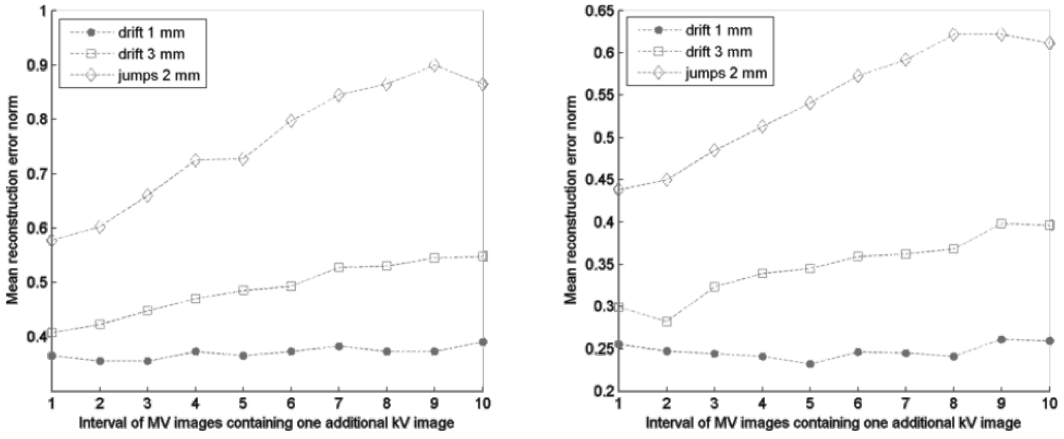

Figure 7: Left: Mean values of the norms of 3D marker reconstruction errors, averaged over all four markers, for the motion patterns of 1 mm drift, 3 mm drift and 2 mm jumps. The frequency of additional kV imaging used for the reconstruction was varied between kV imaging at every gantry angle (interval size 1) to once every 10 MV images. Right: Mean values of the norms of the 3D reconstruction of the mean marker position, for the same motions and parameters.

4 Discussion

The use of markers for motion tracking involves 2D marker detection in MV (and kV) images and 3D reconstruction of the marker positions. Hence, all reported tracking errors are the combination of both 2D detection errors (real for the more realistic motion patterns, simulated otherwise in our experiments) and 3D reconstruction errors. This means that MV images with very low contrast and associated large detection errors can result in large reconstruction errors. The final motion tracking accuracy is generally better than the reconstruction accuracy of each of the separate markers, as the mean 3D marker location should be considered in the end for motion tracking.

As described in Section 2.3, our algorithm enforces a constant AP location of every reconstructed marker around gantry angles of 180^o, 0^o and -180^o for MV-only reconstruction. Additionally, the simulated jump motion patterns used for the validation of the developed algorithms were chosen to contain a jump exactly around 0^o gantry angle. This obviously lead to a large error in the reconstructed marker location at the position of that jump. One can argue that it is better to not enforce a constant marker location and use the originally reconstructed marker location instead. In this case, for this specific situation where the jump motion in the AP location occurs exactly at the moment where this motion is invisible in the MV projection image, the original reconstructions would show a larger (in magnitude), but shorter (in gantry angles) spike in the AP dimension and the global reconstruction error would be smaller. However, in the more general case where large prostate motion does not always occur at exactly this point of the treatment arc, keeping the reconstructed location fixed without the additional spike would correspond better to the actual prostate location, even if the prostate performed a monotonous drift motion (see Figure 4).

Throughout this study, three typical prostate motion patterns were used to examine the results of the proposed detection and reconstruction algorithms. However, real prostate motions can also occur as a superposition of drift and jumps, a motion pattern that was not studied here. Still, we believe that examining each of the components separately is the first required validation step. The results obtained from this are a good indication of our reconstruction method's performance for the separate motion components. The only real difference with a superposed drift and jump motion is then the occurrence of jumps to a possibly larger magnitude away from the base marker location. Results of the 5 mm and 8 mm jump motion patterns in Section 3.2 demonstrate that our reconstruction algorithm also performs well in this case, with the frequency of jumps as high as five in 60 seconds. Therefore, we believe that superposition of drift and jumps would, in the worst case, lead to reconstruction errors comparable to the sum of the separate motion errors. This is still acceptable, given the fact that all reconstruction errors in this study also include 2D detection errors.

Apart from reconstruction accuracy, execution time is also an important factor of performance. The proposed detection and reconstruction algorithms were fully implemented in MATLAB, so the execution speed can therefore still be improved. The current implementation requires 0.2 seconds on an Intel Xeon 2.67 GHz dual processor CPU with 24 GB RAM to process one projection image, i.e. find the estimates of four 2D marker positions, detect these positions and calculate their 3D reconstructions. The possibility of a real-time application of the discussed methods therefore exists if further optimization is performed and the optimized algorithms are implemented in C.

5 Conclusion

An in-house developed 2D detection and 3D reconstruction algorithm was validated on phantom motion data and was used to investigate the effect of additional kV imaging on the accuracy of MV-based marker based prostate motion tracking. Reconstruction errors were examined for simulations of clinical treatment sessions and it was found that additional kV imaging at every gantry angle was not required to obtain good tracking results. Depending on the patient's prostate motion pattern, submillimeter accuracy can be reached with only a dozen additional kV images. When considering the mean marker location, it is even possible to reach submillimeter accuracy without kV imaging.

Acknowledgement

This work was supported by Varian Medical Systems, Inc.

References

[1] Palma D, Vollans E, James K, Nakano S, Moiseenko V, Shaffer R, McKenzie M, Morris J, Otto K. Volumetric modulated arc therapy for delivery of prostate radiotherapy: comparison with intensity-modulated radiotherapy and three-dimensional conformal radiotherapy. *Int J Radiat Oncol Biol Phys.* 2008;72(4):996-1001. doi:10.1016/j.ijrobp.2008.02.047.

[2] Otto K. Volumetric modulated arc therapy: IMRT in a single gantry arc. *Med Phys.* 2008;35(1):310. doi:10.1118/1.2818738.

[3] Crijns W, Budiharto T, Defraene G, Verstraete J, Depuydt T, Haustermans K, Van den Heuvel F. IMRT-based optimization approaches for volumetric modulated single arc radiotherapy planning. *Radiother Oncol.* 2010;95(2):149-52. doi:10.1016/j.radonc.2010.01.012.

[4] Langen KM, Willoughby TR, Meeks SL, Santhanam A, Cunningham A, Levine L, Kupelian PA. Observations on real-time prostate gland motion using electromagnetic tracking. *Int J Radiat Oncol Biol Phys.* 2008;71(4):1084-90. doi:10.1016/j.ijrobp.2007.11.054.

[5] Xie Y, Djajaputra D, King CR, Hossain S, Ma L, Xing L. Intrafractional motion of the prostate during hypofractionated radiotherapy. *Int J Radiat Oncol Biol Phys.* 2008;72(1):236-46. doi:10.1016/j.ijrobp.2008.04.051.

[6] Cramer AK, Haile AG, Ognjenovic S, Doshi TS, Reilly WM, Rubinstein KE, Nabavizadeh N, Nguyen T, Meng LZ, Fuss M, Tanyi JA, Hung AY. Real-time prostate motion assessment: image-guidance and the temporal dependence of intra-fraction motion. *BMC Med Phys.* 2013;13(1):4. doi:10.1186/1756-6649-13-4.

[7] Adamson J, Wu Q. Prostate intrafraction motion assessed by simultaneous kV fluoroscopy at MV delivery II: adaptive strategies. *Int J Radiat Oncol Biol Phys.* 2010;78(5):1323-30. doi:10.1016/j.ijrobp.2009.09.079.

[8] Nederveen a J, Lagendijk JJ, Hofman P. Feasibility of automatic marker detection with an a-Si flat-panel imager. *Phys Med Biol.* 2001;46(4):1219-30.

[9] Mao W, Riaz N, Lee L, Wiersma R, Xing L. A fiducial detection algorithm for real-time image guided IMRT based on simultaneous MV and kV imaging. *Med Phys.* 2008;35(8):3554. doi:10.1118/1.2953563.

[10] Azcona JD, Li R, Mok E, Hancock S, Xing L. Development and clinical evaluation of automatic fiducial detection for tumor tracking in cine megavoltage images during volumetric modulated arc therapy. *Med Phys.* 2013;40(3):031708. doi:10.1118/1.4791646.

[11] Park S-J, Ionascu D, Hacker F, Mamon H, Berbeco R. Automatic marker detection and 3D position reconstruction using cine EPID images for SBRT verification. *Med Phys.* 2009;36(10):4536. doi:10.1118/1.3218845.

[12] Lin W-Y, Lin S-F, Yang S-C, Liou S-C, Nath R, Liu W. Real-time automatic fiducial marker tracking in low contrast cine-MV images. *Med Phys.* 2013;40(1):011715. doi:10.1118/1.4771931.

[13] Poulsen PR, Cho B, Keall PJ. Real-time prostate trajectory estimation with a single imager in arc radiotherapy: a simulation study. *Phys Med Biol.* 2009;54(13):4019-35. doi:10.1088/0031-9155/54/13/005.

[14] Li R, Fahimian BP, Xing L. A Bayesian approach to real-time 3D tumor localization via monoscopic x-ray imaging during treatment delivery. *Med Phys.* 2011;38(7):4205. doi:10.1118/1.3598435.

[15] Slagmolen P, Hermans J, Maes F, Budiharto T, Haustermans K, van den Heuvel F. Fast, accurate, and robust automatic marker detection for motion correction based on oblique kV or MV projection image pairs. *Med Phys.* 2010;37(4):1554. doi:10.1118/1.3355871.

[16] Dehnad H, Nederveen AJ, Heide UA va. der, van Moorselaar RJA, Hofman P, Lagendijk JJW. Clinical feasibility study for the use of implanted gold seeds in the prostate as reliable positioning markers during megavoltage irradiation. *Radiother Oncol.* 2003;67(3):295-302. doi:10.1016/S0167-8140(03)00078-1.

[17] Lim JS. *Two-dimensional signal and image processing.* Englewood Cliffs, NJ, Prentice Hall, 1990, 710 p. 1990-1.

[18] Canny J. A computational approach to edge detection. *IEEE Trans Pattern Anal Mach Intell.* 1986;8(6):679-98. Available at: http://www.ncbi.nlm.nih.gov/pubmed/21869365.

[19] Van Herck H, Crijns W, Slagmolen P, Maes F, Van den Heuvel F, Haustermans K. SU-E-J-138: Fast 2-D Fiducial Marker Detection on Sequential MV Projections in Arc Therapy. *Med Phys.* 2012;39(6):3684. doi:10.1118/1.4734974.

[20] Wiersma RD, Mao W, Xing L. Combined kV and MV imaging for real-time tracking of implanted fiducial markers. *Med Phys.* 2008;35(4):1191. doi:10.1118/1.2842072.

[21] Yue Y, Aristophanous M, Rottmann J, Berbeco RI. 3-D fiducial motion tracking using limited MV projections in arc therapy. *Med Phys.* 2011;38(6):3222. doi:10.1118/1.3584197.

[22] Luenberger DG, Ye Y. *Linear and Nonlinear Programming.* Springer Science & Business Media; 2008:564.

[23] Mor JJ, Thuente DJ. Line search algorithms with guaranteed sufficient decrease. *ACM Trans Math Softw.* 1994;20(3):286-307. doi:10.1145/192115.192132.

[24] Lin Y, Liu T, Yang W, Yang X, Khan MK. The non-Gaussian nature of prostate motion based on real-time intrafraction tracking. *Int J Radiat Oncol Biol Phys.* 2013;87(2):363-9. doi:10.1016/j.ijrobp.2013.05.019.

[25] Ding GX, Duggan DM, Coffey CW. Accurate patient dosimetry of kilovoltage cone-beam CT in radiation therapy. *Med Phys.* 2008;35(3):1135. doi:10.1118/1.2839096.